Article

Multi-Objective Optimization of Deep-Sea Mining Pump Based on CFD, GABP Neural Network and NSGA-III Algorithm

Qiong Hu [1,2], Xiaoyu Zhai [1,2,*] and Zhenfu Li [1,2]

1. School of Mechanical and Electrical Engineering, Central South University, Changsha 410083, China; huqiong@csu.edu.cn (Q.H.); 203711043@csu.edu.cn (Z.L.)
2. State Key Laboratory of Deep Sea Mineral Resources Development and Utilization Technology, Changsha 410012, China
* Correspondence: 203712135@csu.edu.cn; Tel.: +86-188-5007-3387

Abstract: In order to improve the hydraulic performance of a deep-sea mining pump, this research proposed a multi-objective optimization strategy based on the computational fluid dynamics (CFD) numerical simulation, genetic algorithm back propagation (GABP) neural network, and non-dominated sorting genetic algorithm-III (NSGA-III). Significance analysis of the impeller and diffuser parameters was conducted using the Plackett–Burman experiment to filter out the design variables. The optimum Latin hypercube sampling method was used to produce sixty sample cases. The GABP neural network was then utilized to establish an approximate model between the pump's hydraulic performance and design variables. Finally, the NSGA-III was utilized to solve the approximation model to determine the optimum parameters for the impeller and diffuser. The results demonstrate that the GABP neural network can accurately forecast the deep-sea mining pump's hydraulic performance, and the NSGA-III global optimization is effective. On the rated clear water conditions, the optimized pump has a 14.65% decrease in shaft power and a 6.04% increase in efficiency while still meeting the design requirements for the head. Under rated solid-liquid two-phase flow conditions, the head still meets the design requirements, the shaft power is decreased by 15.64%, and the efficiency is increased by 6.00%.

Keywords: multi-objective optimization; deep-sea mining pump; CFD numerical simulation; GABP neural network; NSGA-III

1. Introduction

There are abundant mineral resources on the ocean floor [1]. Investigations into marine mineral resources extraction technology began in the 1950s. So far, it has developed the continuous line bucket system, free-shuttle mining system, vertical pipeline air-lifting technology, and vertical pipeline pump-lifting technology. The vertical pipeline pump-lifting system is the best lifting system for deep-sea minerals taking into account the feasibility and efficiency of the system [2].

The deep-sea mining pump is the key component of the vertical pipeline pump-lifting system and is a multi-stage, high-specific speed centrifugal slurry pump. Its main parts are the centrifugal impeller and space diffuser [3,4]. Deep-sea mining pumps usually use the enlarged flowrate design method to expand the flow path [5] to guarantee the smooth passage of big mineral particles. Deep-sea mining pumps do not work at the design conditions with the enlarged flowrate, which can lead to more vortices and more significant hydraulic loss in the pump flow field, resulting in low head and efficiency [6]. Therefore, after completing the initial design of the pump, the necessary optimization measures should be taken to enhance the head and efficiency.

There are various methods for optimizing pumps. In the early days, optimization methods based on theoretical or empirical formulas were applied to pumps. Oh et al. [7,8] enhanced the mixed-flow pump and the centrifugal pump by establishing mathematical

models of the efficiency and net positive suction head (NPSH). Yang [9] modified a centrifugal pump using a hydraulic loss mathematical model. The design of experiment (DOE) methods could be utilized to comprehend the relationship between process and product parameters and response characteristics. Many DOE methods have been applied to the optimization of pumps. Pei [10] improved the required NPSH of the pump by 0.63 m based on orthogonal DOE. Ayremlouzadeh [11] used Taguchi DOE to determine the optimum impeller parameters for a low-speed centrifugal pump. Heo [12] enhanced a mixed-flow pump's efficiency by 1.36% using the response surface method (RSM). Hong [13] decreased the impeller average wear intensity by 29.5% applying the RSM.

The above studies are mostly single-objective optimization studies of pumps. Single-objective optimization can only enhance a single aspect of the pump's performance and cannot satisfy the design requirements. In recent years, with the development of multi-objective optimization algorithms [14,15], various algorithms have been utilized to optimize pumps. Multi-objective optimization algorithms include traditional and intelligent algorithms [16]. By introducing weights, traditional multi-objective optimization algorithms commonly turn a multi-objective optimization task into a single-objective optimization task. The optimization effect of the algorithm is not good due to the problem of additional weight idealization. Intelligent optimization algorithms mainly include the particle swarm optimization (PSO) algorithm, ant colony algorithm (ACA), and genetic algorithm (GA). These algorithms can perform global optimization in the range of all design variables, which can better capture the spirit of multi-objective optimization. Nourbakhsh [17] and Gan [18,19] performed multi-objective optimization of centrifugal pumps by the PSO algorithm, demonstrating the feasibility of the PSO algorithm for pump optimization. Zhang [20] combined a BP neural network with the NSGA-II to increase the pressure rise of a helicon-axial multiphase pump by 10% and the efficiency by 3%. The inducer of a centrifugal pump was optimized by Shojaeefard [21] using the neural network and NSGA-II. The head coefficient, efficiency, and required NPSH of the modified pump rose by 14.3%, 0.3%, and 30.2%, respectively. Xu [22] modified a jet pump utilizing the NSGA-II and radial basis function (RBF) neural network. The head of the modified pump is enhanced by 30.46%, and its efficiency is marginally improved.

In summary, multi-objective optimization algorithms are primarily applied to single-stage radial-flow centrifugal pumps for single-phase flow. However, there is almost no multi-objective optimization investigation for multi-stage axial-flow deep-sea mining slurry pumps. The subject of this investigation is the six-stage deep-sea mining slurry pump designed by Central South University. Based on the numerical simulation, the NSGA-III is utilized to solve the approximation model of the hydraulic performance established through the GABP neural network. In this way, the pump's impeller and diffuser are optimized to decrease the shaft power and increase the efficiency while the head meets the design requirements.

2. Structure and Key Parameters of Deep-Sea Mining Pump

The structure of the six-stage deep-sea mining pump is displayed in Figure 1. The deep-sea mining pump is manufactured as a vertical multistage pump with centrifugal impellers and space diffusers to guarantee the features of high head and axial flow. Table 1 displays the pump's design parameters under the rated operating circumstances. At the pump's rated operating conditions, the rotational speed n is 1450 rpm, the specific speed n_s is 150, the flowrate Q is 420 m^3/h, the shaft power P is 680 kW, the head H is 270 m, the efficiency η is 52%, the volume concentration of conveyed particles C_v is 5%, and the average diameter of conveyed particles $\overline{\Phi}$ is 10 mm.
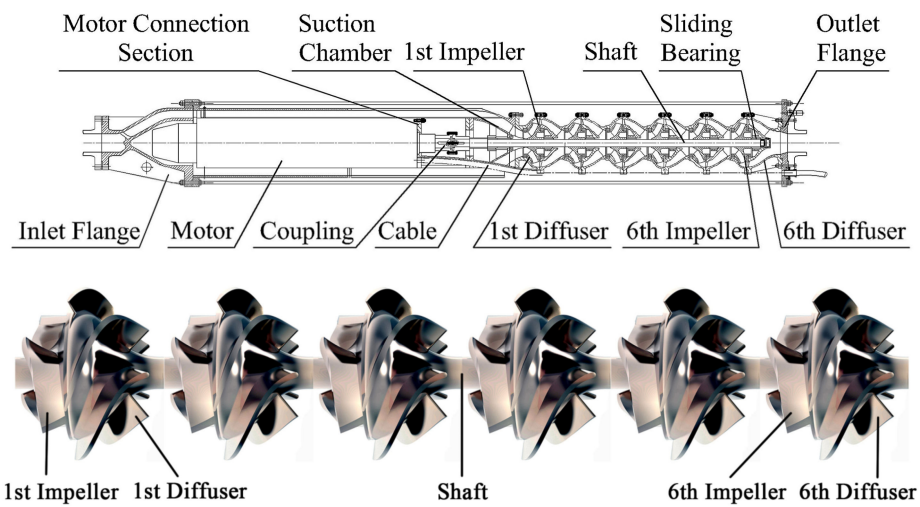
Figure 1. Structure of the deep-sea mining pump.

Table 1. The main parameters of the impeller and diffuser.

Structure of Impeller	Parameter	Structure of Diffuser	Parameter
Number of blades Z_1	4	Number of blades Z_2	5
Blade outlet width b_2	60 mm	Blade inlet width b_3	62 mm
Inlet diameter D_1	235 mm	Maximum diameter of the internal streamline D_3	395 mm
Average outlet diameter D_{2m}	410 mm	Maximum diameter of the external streamline D_4	516 mm
Outlet blade thickness δ_2	15 mm	Outlet diameter D_5	235 mm
Blade wrap angle ϕ_1	110°	Inlet blade thickness δ_3	7 mm
Inlet blade angle β_1	35°	Blade wrap angle ϕ_2	95.5°
Outlet blade angle β_2	32.5°	Inlet blade angle α_3	12°
Shaft diameter d	95 mm	Outlet blade angle α_4	85°

The centrifugal impeller and space diffuser are the critical components of the deep-sea mining pump. The impeller converts mechanical energy into kinetic, pressure, and potential energy of the slurry by its rotation. The diffuser collects the slurry at the impeller outlet and converts the kinetic energy into pressure energy. Therefore, the impeller and diffuser decide the pump's hydraulic performance and are the subject of optimization in this study. Figure 2 shows the meridional contour and blade profile of the impeller and diffuser. The key parameters of the impeller and diffuser are displayed in Table 1.
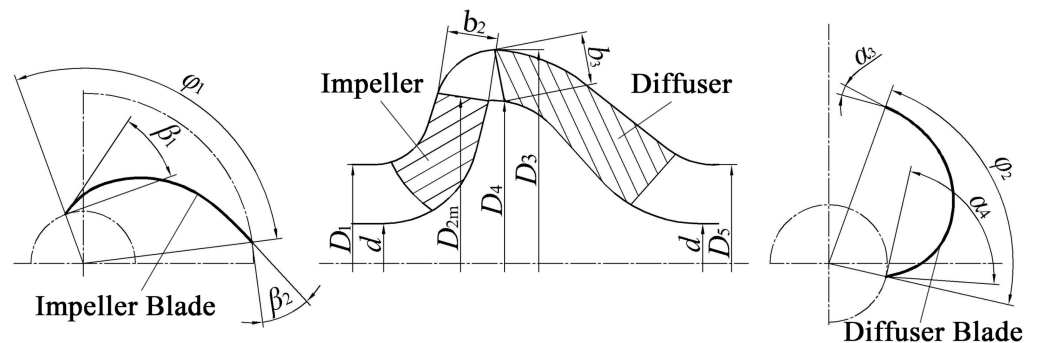
Figure 2. Meridional contour and blade profile of the impeller and diffuser.

3. Numerical Simulation and Experimental Validation

3.1. Basic Assumptions

When the volume concentration of particles conveyed by centrifugal pumps is less than 20%, the external characteristics of pumps are similar under clear water and solid-

liquid two-phase flow conditions [23]. As a result, deep-sea mining pumps are usually designed in clear water conditions, and then particle conveying experiments are conducted to evaluate the performance of the pump in transporting mineral particles. Following the design principle, the optimization task of the deep-sea mining pump in this investigation is also conducted under clear water conditions. The pump's hydraulic performance for conveying mineral particles is also tested after optimization.

Numerical simulations of the pump under both conditions were completed in ANSYS Fluent 2021R1 software. During the simulations, the following assumptions were made:

(1) The physical characteristics of solids and liquids are steady, and there are no phase changes.
(2) Fluids are incompressible
(3) The conveyed particles are spherical, uniformly sized particles.

3.2. Boundary Conditions and Computational Settings

The numerical simulation under clear water conditions is based on a pressure-based steady-state solution. The clear water has a density of 998.2 kg/m^3 and a viscosity of 0.001003 kg/(m·s). The impeller spinning fluid domain is represented by the multiple reference frame (MRF) model. The renormalization group *k-ε* (RNG *k-ε*) turbulence model is chosen to simulate the complex rotating fluid. Standard wall functions handle industrial fluids with a y^+ of 15–100. Velocity inlet and pressure outlet are the boundary conditions. The solution methods of the SIMPLEC and second order upwind scheme are selected to improve calculation accuracy. The absolute criteria of residual monitors are set to 1×10^{-4}. The number of iteration steps is 3000. Take the simulation results from the last calculation cycle to calculate the pump's hydraulic performance.

Given the conditions of marine mineral particles conveying at low volume concentrations (5–10%), the computational fluid dynamics and discrete phase model (CFD-DPM) model based on the Euler–Lagrange theory is utilized to simulate the solid-liquid two-phase flow. The DPM model is commonly used to deal with the problem of particles with volume concentrations less than 10%. The above method is implemented through the discrete phase model in the FLUENT software. The particles are spherical with a diameter of 10 mm and a density of 1910 kg/m^3, considering the Saffman force, fluid drag force, pressure gradient force, and virtual mass force of particles.

The head *H*, shaft power *P*, and efficiency *η* of the deep-sea mining pump are calculated as follows:

$$H = \frac{p_2 - p_1}{\rho g} + (z_2 - z_1) \tag{1}$$

where p_1 and p_2 are the total pressure of the inlet and outlet, z_1 and z_2 are the height of the inlet and outlet, ρ is the fluid density, and *g* is the gravitational acceleration.

$$P = \omega M \tag{2}$$

where ω is the angular velocity of the pump, and *M* is the moment of the impeller.

$$\eta = \frac{\rho g Q H}{P} \tag{3}$$

where *Q* is the volume flowrate of fluid.

3.3. Modeling and Meshing of Flow Domain

In addition to the primary impeller and diffuser fluid domain, the computational model for the pump also adds the fluid domain of the inlet and outlet pipe. These pipes' length is five times the hydraulic diameter of the inlet or outlet, which allows turbulence at the pump inlet and outlet to develop fully. All fluid domains are divided into unstructured meshes using ANSYS ICEM CFD 2021R1 software, and the divided meshes are shown in Figure 3.
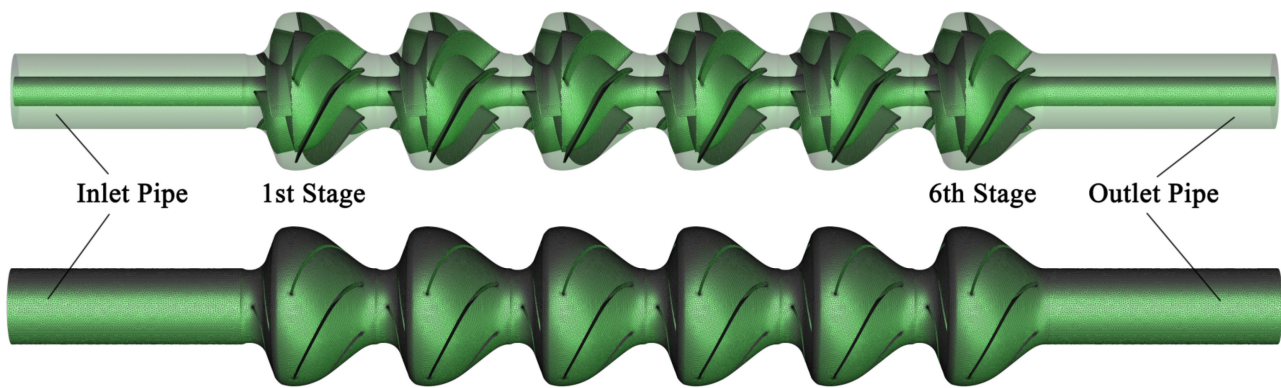
Figure 3. Meshes of the deep-sea mining pump.

A grid independence analysis of meshes was performed to increase computation precision, as indicated in Table 2. In order to evaluate the discretization error of the CFD method, the grid convergence index (GCI) is calculated using Celik's method [24]. Three meshes with $N_1 = 10{,}924{,}128$, $N_2 = 4{,}673{,}330$, and $N_3 = 1{,}911{,}196$ were selected to calculate GCI values. The grid refinement factor r_{21} is 1.327, and r_{32} is 1.347. The head is set as the variable ϕ. The final calculated GCI$_{21}$ is 2.19%, and GCI$_{32}$ is 0.87%, which meets the convergence requirements. The computed hydraulic performance parameters of the pump almost stop varying when the number of meshes approaches 10.92 million. Given the calculation speed, the number of meshes for all calculation models was estimated to be about 11 million. The minimum orthogonal quality value of meshes is 0.4. The maximum skewness value of meshes is 0.84. The value of y^+ is approximately 50 for the RNG k-ε turbulence model and standard wall functions.

Table 2. Grid independency analysis.

Number of Meshes	Head (m)	Shaft Power (W)	Efficiency (%)
1,911,196	308.72	798,476	44.17
4,673,330	305.36	756,628	45.99
8,042,426	300.47	738,391	46.49
10,924,128	297.70	687,891	49.44
13,808,964	297.87	691,724	49.20

3.4. Experimental Verification in Clean Water Conditions

To verify the accuracy of the numerical simulations under clear water conditions, the pump's hydraulic performance was tested in the laboratory of Premier Electric Pump Co., Ltd. in Tianjin, China. Figure 4 depicts the layout of the clear water experimental system. The experimental system consists of the pump, pipe system, temperature sensor, pressure sensor, electromagnetic flowmeter, and electromagnetic valve. The design of the experimental system conforms to Chinese national standards, and the measurement methods and accuracy of the test parameters conform to the relevant regulations.
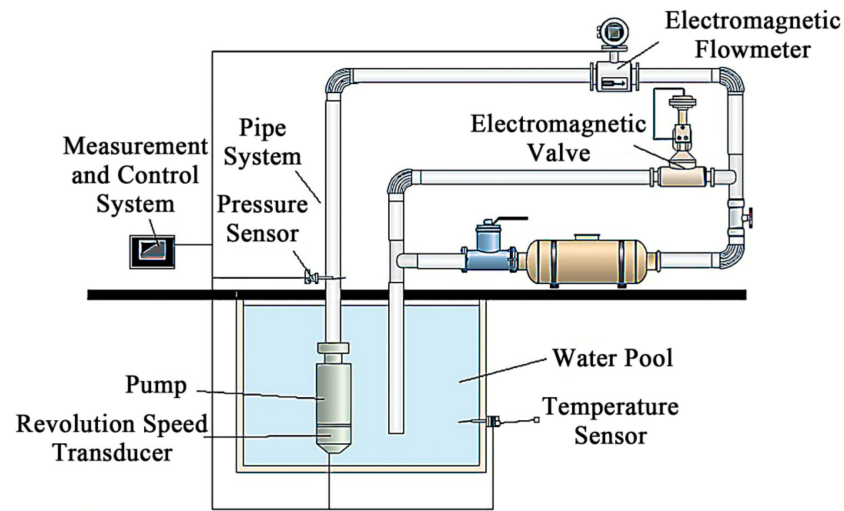
Figure 4. Layout of the clear water experimental system.

The hydraulic performance of the deep-sea mining pump in the flow range of 50–700 m^3/h at rated speed (n = 1450 rpm) was measured. Figure 5 illustrates the comparison of the CFD simulated and experimental results. The trend of the simulation results and the experimental results are the same on the whole, and the values basically match. The maximum relative error of the simulated shaft power was 4.87%. The relative errors of the simulated head and efficiency are only significant in the lower flow rate (Q < 200 m^3/h) conditions, 4.46–7.43%, and 6.59–9.74%, respectively. In comparison, the relative errors in the other conditions are all controlled by 4.42%.
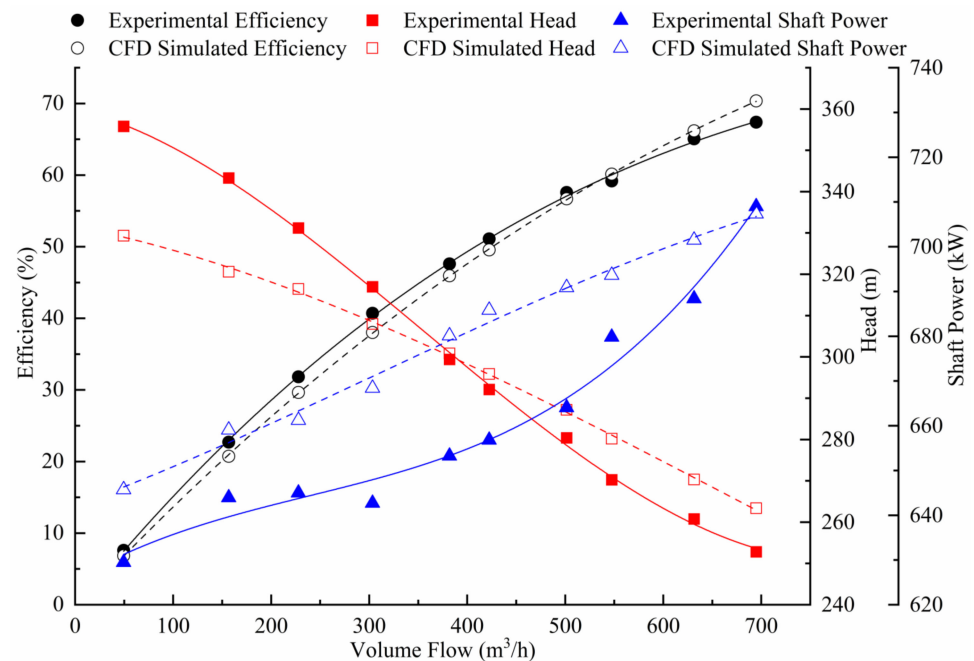
Figure 5. Comparison of the CFD simulated and experimental results.

The significant errors of numerical simulations at the extreme conditions do not affect the optimization work in this research, as the optimization work was carried out at the rated flowrate (420 m^3/h). The comparison of the simulated and experimental results at rated conditions is shown in Table 3. It can be concluded that the numerical simulations at rated clear water conditions are very reliable.

Table 3. Comparison of the experimental and CFD simulated results at rated conditions.

	Head (m)	Shaft Power (W)	Efficiency (%)
Experimental Results	292.50	656,672	50.89
CFD Simulated Results	297.85	686,866	49.54
Relative Errors	1.83%	4.60%	2.65%

3.5. Experimental Verification in Solid-Liquid Two-Phase Flow Conditions

The slurry conveying experiment of the deep-sea mining pump was completed at the State Key Laboratory of Deep-sea Mineral Resources Development and Utilization Technology in Changsha, China. Figure 6 depicts the layout of the slurry conveying experimental system. The system consists of the pump being tested, the pipe system, the hydraulic feeder, the pressure sensor, the electromagnetic flowmeter, and the electronical ball valve.
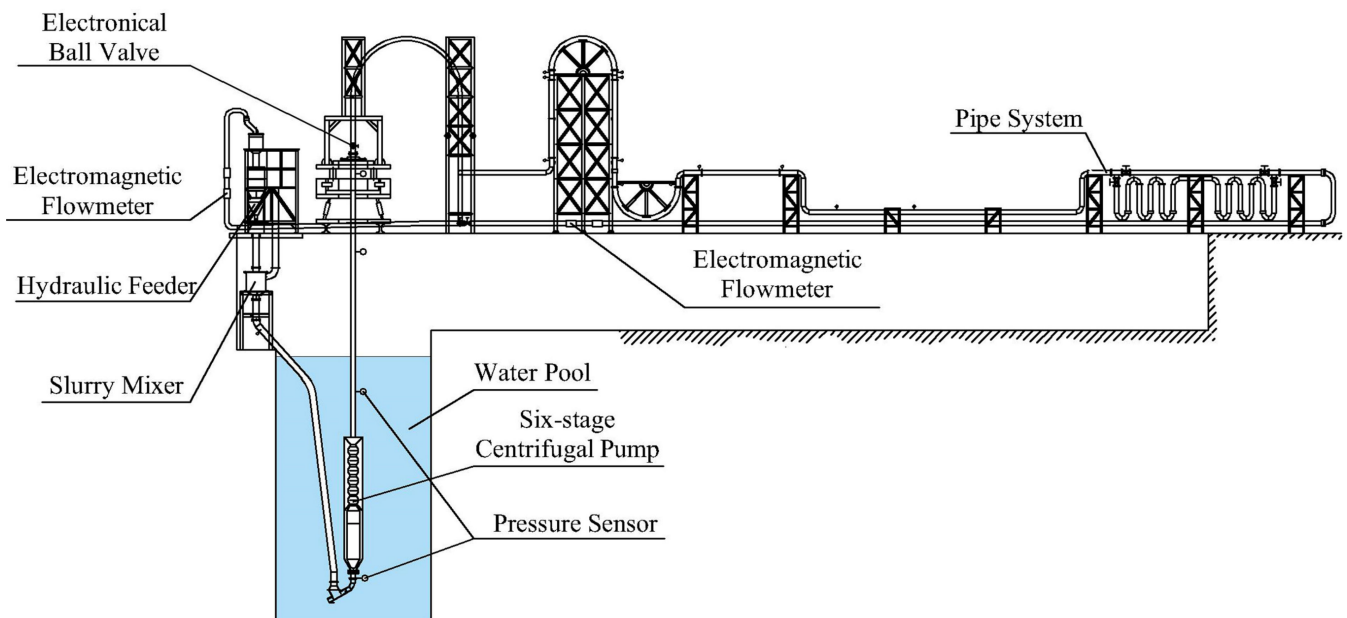

Figure 6. Layout of the slurry conveying experimental system.

Due to the limited pressure loading capacity of the experimental system, all slurry conveying tests were carried out at 900 r/min operating conditions. Four sets of test data with different particle volume concentrations were obtained. Table 4 illustrates the comparison of the experimental and CFD-DPM simulated results. When the volume concentration of the conveyed particles is low, the simulation results have a slight error of around 1%. Since the volume concentration of particles under the deep-sea mining pump's rated conditions is 5%, the DPM model is a good fit for the numerical simulation.

Table 4. Comparison of the experimental and CFD-DPM simulated results.

Volume Flow (m³/h)	Volume Concentration of Particles (%)	Head of Experiment Results (m)	Head of CFD-DPM Simulated Results (m)	Relative Errors (%)
429.41	3.56	99.08	100.05	0.98
452.90	4.69	98.8	97.68	1.13
468.31	5.52	97.14	97.17	0.03
425.42	9.01	99.42	96.11	3.33

4. Approximate Model of Hydraulic Performance Using GABP Neural Network

4.1. Design Variables Selection

Studies [25,26] have shown that there is a rotor–stator interaction between the impeller outlet and the diffuser inlet of a centrifugal pump, which makes the turbulent kinetic energy locally high and the vortex loss serious. Therefore, it is vital to concentrate on optimizing the impeller outlet and diffuser inlet.

There are plenty of parameters at the impeller outlet and diffuser inlet, but they have different significances of effect on the hydraulic performance. The Plackett–Burman experimental design and analysis were performed using Minitab software to screen out the parameters that significantly affect the optimization objectives. The Plackett–Burman experiment requires only N + 1 trials of the N test factors to determine the significance of the effect of each factor on the test results. The optimization objectives are the head, shaft power, and efficiency of the deep-sea mining pump under the rated conditions. The impeller parameters screened are the D_{2m}, b_2, δ_2, and β_2. The diffuser parameters screened are the b_3, δ_3, and α_3. In addition, four dummy factors, X_1, X_2, X_3, and X_4, are added for error analysis. Twelve trials were performed with each of the eleven parameters at both high and low levels. Table 5 displays the experimental design scheme. Table 6 displays the simulated results for each set of experiments.

Table 5. Plackett–Burman experimental design scheme.

Number	D_{2m} (mm)	b_2 (mm)	δ_2 (mm)	β_2 (°)	b_3 (mm)	δ_3 (mm)	α_3(°)	X_1	X_2	X_3	X_4
1	420	72	10	40	72	10	8	−1	−1	1	−1
2	400	72	20	20	72	10	20	−1	−1	−1	1
3	420	60	20	40	60	10	20	1	−1	−1	−1
4	400	72	10	40	72	5	20	1	1	−1	−1
5	400	60	20	20	72	10	8	1	1	1	−1
6	400	60	10	40	60	10	20	−1	1	1	1
7	420	60	10	20	72	5	20	1	−1	1	1
8	420	72	10	20	60	10	8	1	1	−1	1
9	420	72	20	20	60	5	20	−1	1	1	−1
10	400	72	20	40	60	5	8	1	−1	1	1
11	420	60	20	40	72	5	8	−1	1	−1	1
12	400	60	10	20	60	5	8	−1	−1	−1	−1

Table 6. CFD simulated results of the Plackett–Burman experiment.

Number	1	2	3	4	5	6	7	8	9	10	11	12
Head (m)	325.46	275.29	308.87	293.66	262.79	279.34	290.55	309.9	301.02	304.76	299.5	271.25
Shaft Power (W)	786,792	618,388	698,590	780,995	498,929	617,009	604,301	676,644	675,001	662,310	669,510	516,380
Efficiency (%)	47.26	50.86	50.51	42.96	60.17	51.72	54.93	52.32	50.95	52.57	51.11	60.01

The regression equations in terms of coded factors for the head, shaft power, and efficiency can be established from the experimental results in Tables 5 and 6. The regression coefficients and significance test results (one-tailed probability *p*-values) for every factor are displayed in Table 7.

Table 7. Regression coefficients and significance test results.

Factors	Regression Coefficients of Head	*p*-Values of Head	Regression Coefficients of Shaft Power	*p*-Values of Shaft Power	Regression Coefficients of Efficiency	*p*-Values of Efficiency
D_{2m}	12.35	0.0012	34,735.58	0.0075	−0.9342	0.1406
b_2	8.15	0.0055	49,617.58	0.0020	−2.63	0.0067
δ_2	−1.49	0.3746	−13,282.75	0.1282	0.5808	0.3179
β_2	8.40	0.0050	52,130.25	0.0017	−2.76	0.0056
b_3	−2.32	0.1954	9415.08	0.2465	−0.8992	0.1523
δ_3	0.0758	0.9620	−1012.08	0.8911	0.0258	0.9620
α_3	−2.08	0.2374	15,309.92	0.0921	−1.79	0.0245

A positive regression coefficient value may indicate a positive correlation between the optimization objective and the factor. A negative value may mean that the optimization objective and the factor are negatively correlated. The bigger the absolute value of the regression coefficient, the more significant the effect of the factor on the optimization target. The *p*-value can quantitatively evaluate the significance of a factor's influence. When a factor's *p*-value is less than 0.05, the factor is regarded as a significant influence; when the *p*-value is greater than 0.1, the factor is regarded as a non-significant influence, indicating that it does not influence the optimization target; when the *p*-value is between 0.05 and 0.1, the factor is regarded as a sub-significant influence.

The results of the significance analysis show that the significant influencing factors of head and shaft power are the D_{2m}, b_2, and β_2. The significant influencing factors of efficiency are the b_2, β_2, and α_3. Taking all factors into account, the optimized design variables are the D_{2m}, b_2, β_2, and α_3. According to the design requirements and experience of deep-sea mining pumps, the optimized design variables are determined in the range of values, as shown in Table 8.

Table 8. Range of values for design variables.

Design Variables	Range of Value	Original Value
Average outlet diameter of the impeller D_{2m}	[395 mm, 425 mm]	410 mm
Impeller outlet width b_2	[60 mm, 75 mm]	60 mm
Outlet blade angle of the impeller β_2	[20°, 40°]	32.5°
Inlet blade angle of the diffuser α_3	[8°, 20°]	12°

4.2. Establishing Sample Database

The amount of training samples for a neural network is at least ten times the amount of variables in the input layer [27], and the sample points should be evenly distributed within the variable interval. The optimum Latin hypercube sampling (OLHS) approach is a modified approach of Latin hypercube sampling (LHS) that considers the uniformity of the distribution of sample points. The sample space obtained by the OLHS will have very good space-filling ability. A comparison of the effects of the two sampling methods is shown in Figure 7. Sixty sets of design variable samples generated by the OLHS method are presented in Table A1.
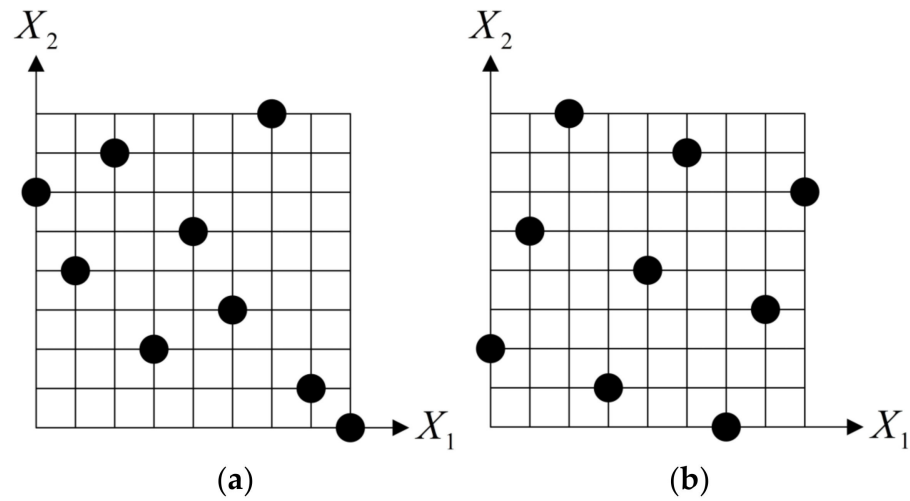
Figure 7. Comparison of the sampling effects of LHS and OLHS: (**a**) LHS; (**b**) OLH.

4.3. Fitting and Prediction of GABP Neural Network

Figure 8 reveals the basic structure of the back propagation (BP) neural network [28]. In Figure 8, X_i is the input of the neuron, w_{ij} and w_{jk} are the connection weights, and b_j and b_k are the thresholds of the neuron in the input layer and output layer. If the activation functions of the neurons in the hidden layer and output layer are f_1 and f_2, respectively, the output Y_i of the BP neural network is:

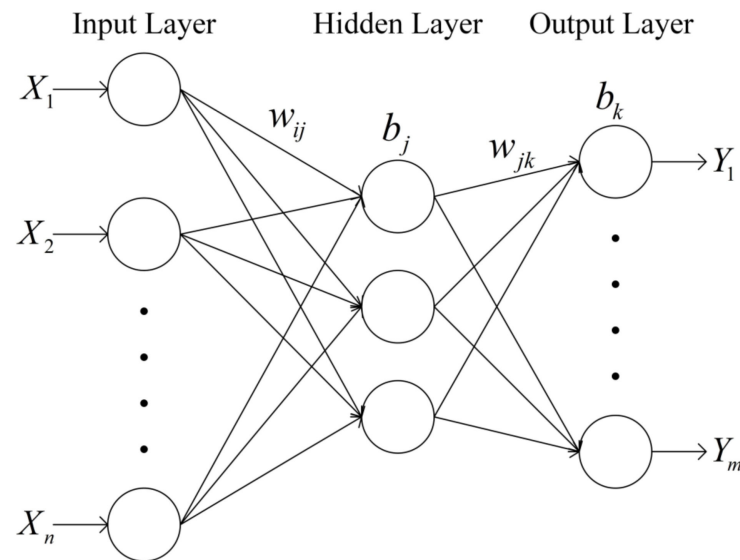$$Y_i = f_2[w_{jk}f_1(w_{ij}X_i - b_j) - b_k] \tag{4}$$

Figure 8. Basic structure of the BP neural network.

The BP neural network's basic principle allows the weights and thresholds to converge to a specific value, but this does not ensure that it is a global minimum in the error plane, which may get into the problem of local minima and lead to poor performance of the BP neural network.

The genetic algorithm (GA) [29,30] can search for the optimum solution globally. It can continuously select individuals of the population through selection, crossover, and mutation. Individuals with a better fitness value are ultimately preserved to achieve the globally optimum solution. Therefore, the weights and thresholds can be modified by the GA to make it less likely to fall into local minima so that the performance of the BP

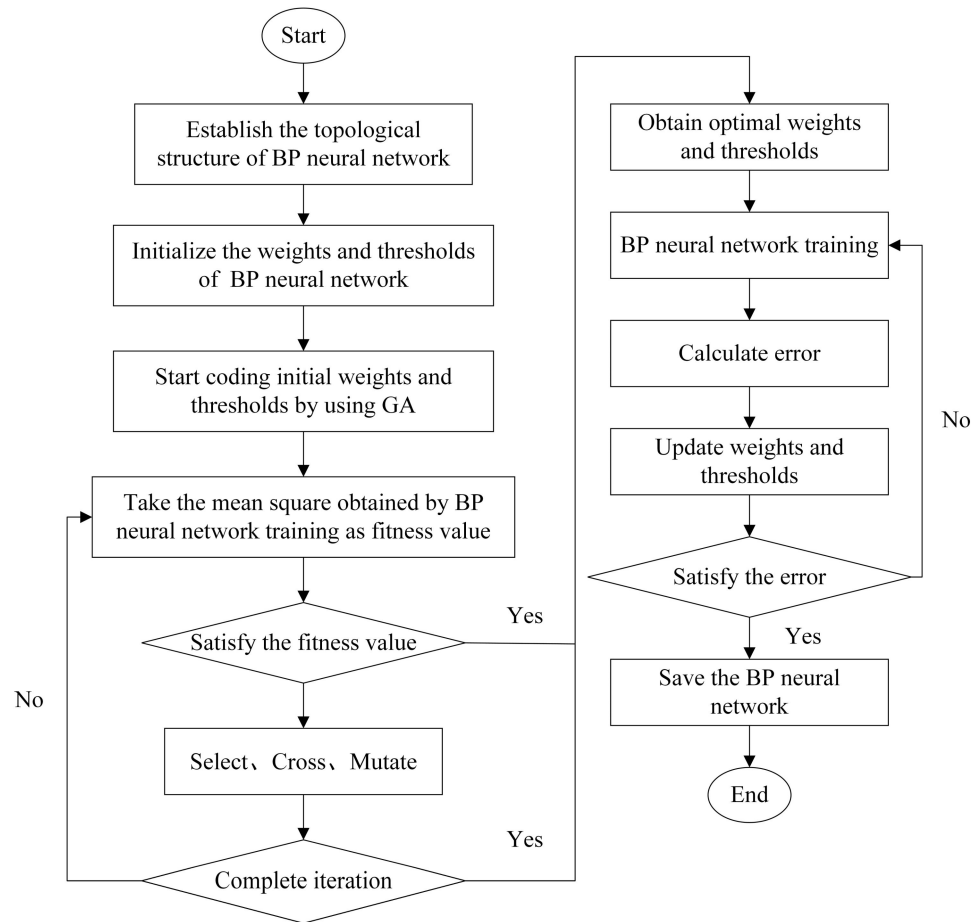neural network can be improved. The flowchart of the GABP neural network is displayed in Figure 9.

Figure 9. Flowchart of the GABP neural network.

The fitting of the BP and GABP neural network was carried out by randomly selecting 50 out of 60 samples as the training samples. The remaining ten samples were utilized as the test samples to evaluate the prediction work. The neural network's performance is assessed by the coefficient of determination (R^2) and mean relative error (MRE). The R^2 can evaluate the approximate degree of the neural network approximation model, and the closer its value is to 1, the higher the approximate degree. The R^2 and MRE are defined as follows:

$$R^2 = 1 - \frac{\sum\limits_{i=1}^{N}(y_o - y_i)^2}{\sum\limits_{i=1}^{N}(y_i - \overline{y}_i)^2} \tag{5}$$

$$MRE = \frac{1}{N}\sum_{i=1}^{N}\frac{|y_o - y_i|}{y_i} \tag{6}$$

where y_o is the output value of the neural network, y_i is the CFD simulated value, $\overline{y}_i$ is the average of the CFD simulated values, and N is the amount of data.

The results of fitting and prediction for the head, shaft power, and efficiency are shown in Figure 10. The MRE and R^2 of the fitting are shown in Table 9. It is evident that the fitting performance of the GABP neural network is much better than that of the BP neural network. The MRE of the GABP neural network is 0.65% at most, and the R^2 is all greater

than 0.98, which indicates that the prediction accuracy of the GABP neural network will be very high.

Table 9. Comparison of the MRE and R^2 of fitting.

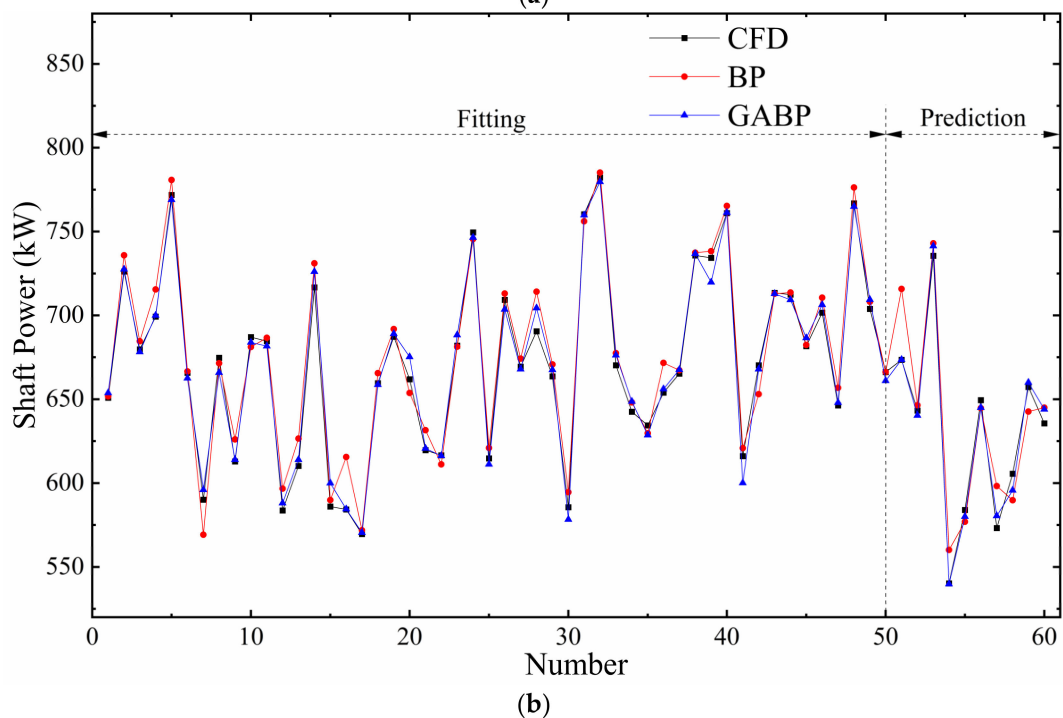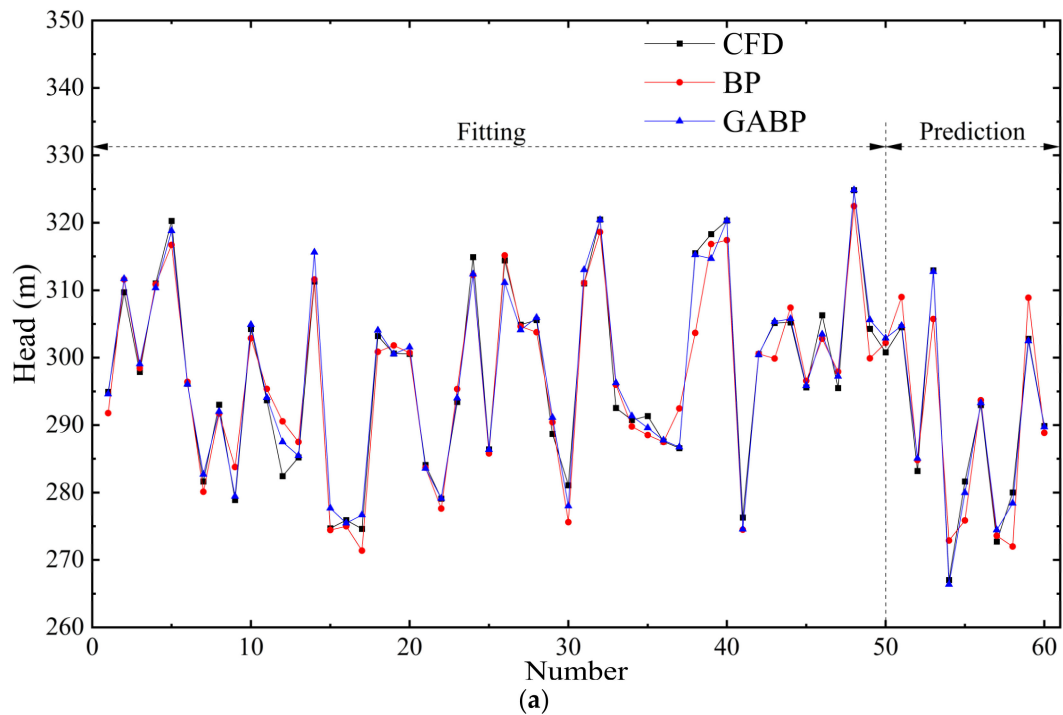| Neural Network	MRE of Head	R^2 of Head	MRE of Shaft Power	R^2 of Shaft Power	MRE of Efficiency	R^2 of Efficiency
BP	0.75%	0.9465	1.15%	0.9661	0.66%	0.9514
GABP	0.43%	0.9827	0.65%	0.9881	0.29%	0.9863

(**a**)
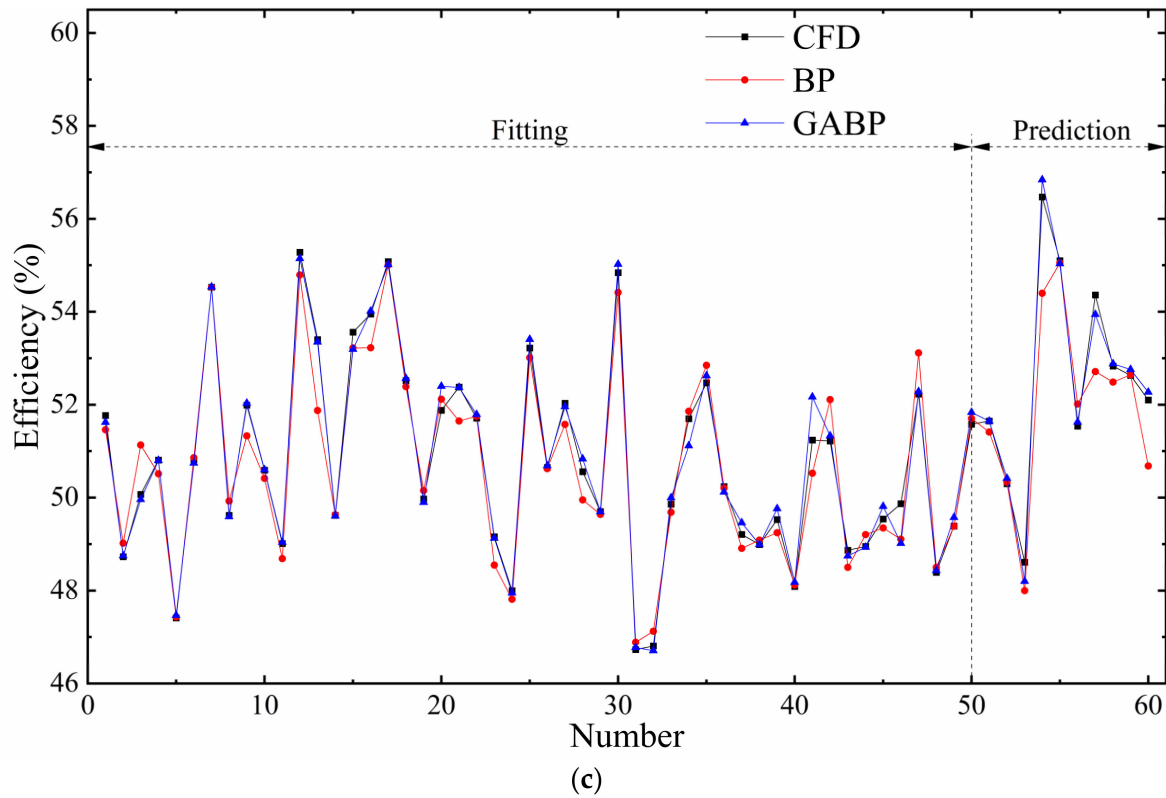

(**b**)

Figure 10. *Cont.*

Figure 10. Comparison of the performance of the BP and GABP neural network: (**a**) Head; (**b**) Shaft Power; (**c**) Efficiency.

The MRE of the prediction is shown in Table 10. The results show that the prediction effect of the GABP neural network is also improved, with a maximum MRE of 0.73%. Therefore, the approximate model between the hydraulic performance and design variables of the deep-sea mining pump is constructed by GABP neural network.

Table 10. Comparison of the MRE of the prediction.

Neural Network	MRE of Head	MRE of Shaft Power	MRE of Efficiency
BP	1.44%	2.41%	1.29%
GABP	0.31%	0.73%	0.34%

5. Multi-Objective Optimization Based on NSGA-III

The objectives of the multi-objective optimization of the deep-sea mining pump are to achieve the maximum head, minimum shaft power, and maximum efficiency within the range of values of the design variables. The mathematical expression of the multi-objective optimization problem is as follows:

$$\begin{cases} Maximize H = f_1(D_{2m}, b_2, \beta_2, \alpha_3) \\ Minimize P = f_2(D_{2m}, b_2, \beta_2, \alpha_3) \\ Maximize \eta = f_3(D_{2m}, b_2, \beta_2, \alpha_3) \end{cases} \tag{7}$$

where $D_{2m} \in [395, 425 \text{ mm}]$, $b_2 \in [60, 75 \text{ mm}]$, $\beta_2 \in [20°, 40°]$, and $\alpha_3 \in [8°, 20°]$.

Deb [31] proposed the NSGA-II in 2000. The NSGA-II can maintain the diversity of populations by introducing the elitist preserving approach and the crowding distance assignment approach. However, the amount of non-dominated individuals in the population grows exponentially when the number of optimization objectives increases. The crowding distance approach is inefficient as a diversity-preserving operator and even returns an

ambiguous value. Therefore, the NSGA-II is mainly used for two-objective optimization problems. To address these problems, Deb et al. [32,33] also proposed the NSGA-III algorithm based on the selection mechanism of reference points in 2014. Figure 11 displays the flowchart for the NSGA-III.
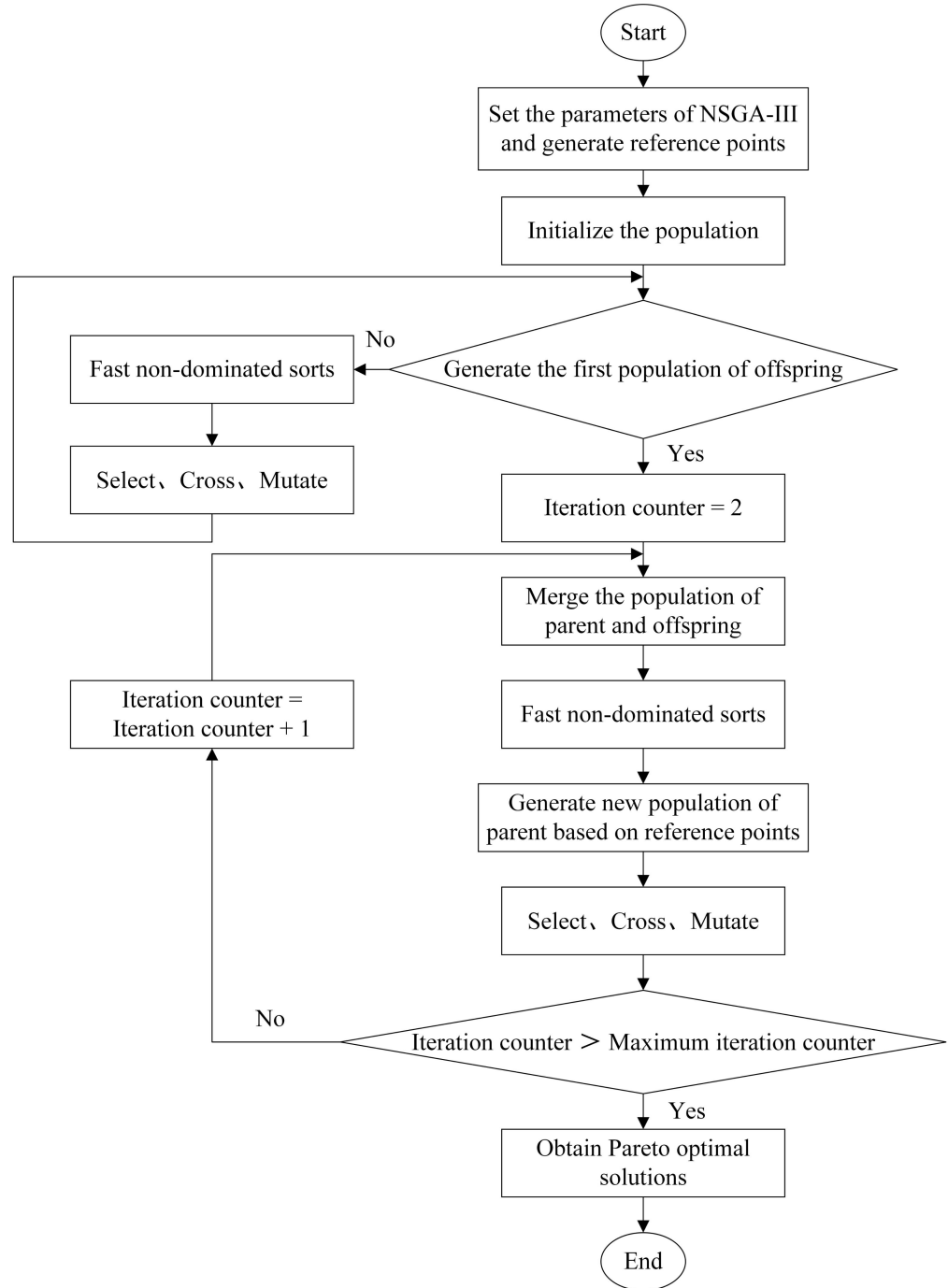

Figure 11. Flowchart of the NSGA-III.

The framework of NSGA-III is similar to that of NSGA-II, except that the critical layer selection method of NSGA-III uses the reference point approach. As a result, the population obtained by NSGA-III has better distributivity. The time complexity and convergence of the NSGA-III are also enhanced, making it perfect for handling optimization problems with three or more objectives. In this research, the NSGA-III is chosen to solve the approximate

model of the deep-sea mining pump. The basic parameters of the NSGA-III are displayed in Table 11.

Table 11. Basic parameters of the NSGA-III.

Parameter	Value
Number of reference points	200
Number of generations	1000
Population size	200
Crossover probability	0.09
Mutation probability	0.05

6. Results and Discussion

6.1. Pareto Optimal Frontiers Analysis

After 1000 genetic iterations of NSGA-III, the Pareto optimal frontiers containing 200 populations were obtained, as shown in Figure 12. All the Pareto optimal solutions are distributed on a banded spatial surface, which covers each head point, shaft power point, and efficiency point. These points are rarely distributed in spatial regions with lower efficiency and higher shaft power. They are more evenly distributed in the regions with superior overall performance, reflecting the good multi-objective global optimization capability of NSGA-III.
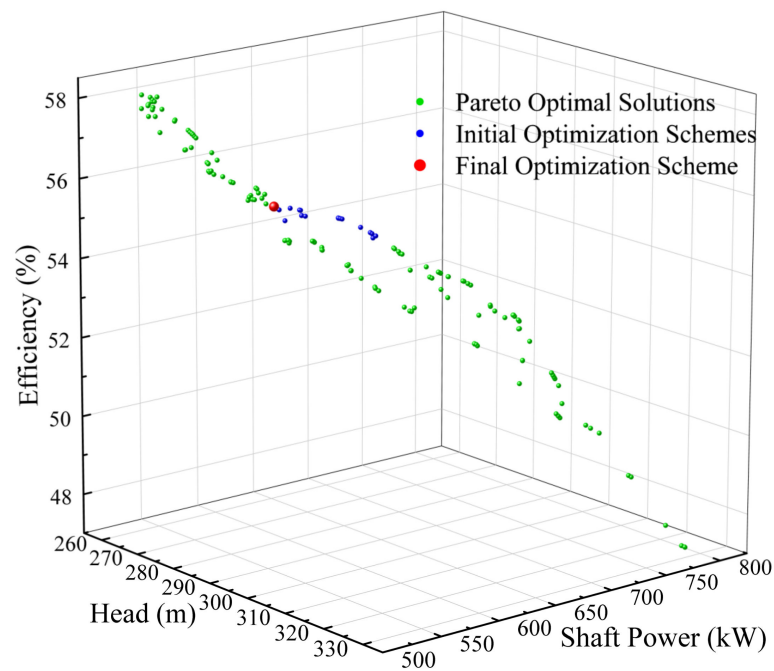

Figure 12. Pareto optimal frontiers.

From the 200 non-dominated optimal solutions, 25 initial optimization schemes were obtained by initial screening with head $H \geq 1.05 \times 270$ mm, shaft power $P \leq 640$ kW, and efficiency $\eta \geq 55\%$. From these 25 initial optimization schemes, the one with the highest efficiency was selected as the final optimization scheme. A comparison of the design variables of the final optimized pump with the original pump is displayed in Table 12. Compared to the original pump, the final optimized pump has an increased impeller outlet width and inlet blade angle of the diffuser, and a reduced average outlet diameter of the impeller and outlet blade angle of the impeller.

Table 12. Comparison of the impeller and diffuser parameters of the optimized pump with the original pump.

Design Variables	The Original Pump	The Final Optimized Pump
Average outlet diameter of the impeller D_{2m}	410 mm	408.73 mm
Impeller outlet width b_2	60 mm	61.47 mm
Outlet blade angle of the impeller β_2	32.5°	20.00°
Inlet blade angle of the diffuser α_3	12°	13.68°

6.2. Comparative Analysis in Clear Water Conditions

Numerical simulations were completed for the final optimized pump under rated clear water conditions. Table 13 illustrates the comparison of the hydraulic performance of the original and final optimized pump. The results show that the relative errors in the prediction of the head, shaft power, and efficiency of the final optimized pump by the GABP neural network are 0.55%, 1.65%, and 0.19%, respectively. The optimized deep-sea mining pump has a reduction in shaft power of 100,607 W (14.65%) and an increase in efficiency of 6.04% while meeting the design requirements for the head.

Table 13. Comparison of the hydraulic performance of the original and final optimized pump.

	Head of GABP	Shaft Power of GABP	Efficiency of GABP	Head of CFD	Shaft Power of CFD	Efficiency of CFD
The original pump	-	-	-	297.85 m	686,866 W	49.54%
The final optimized pump	283.68 m	576,750 W	55.69%	285.23 m	586,259 W	55.58%

Figure 13 shows the streamlines on the shaft cross-section of the original and optimized pumps. It is clear that the direction of the flow field is generally stable in both pumps. However, there are many vortices at the impeller outlet and diffuser inlet. Figure 14 shows the streamlines on the cross-section at the transition between the impeller outlet and the diffuser inlet. The results reveal that the optimized pump's flow field has improved significantly, with a more stable flow direction and a reduction in vortices.
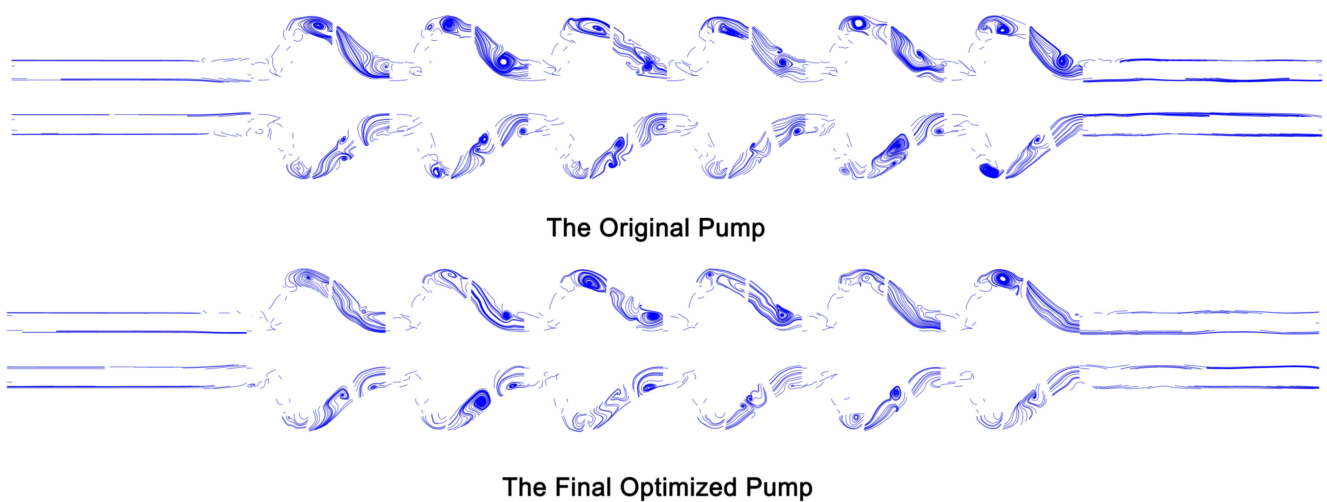

The Original Pump

The Final Optimized Pump

Figure 13. The streamlines on the shaft cross-section of the original and optimized pumps.
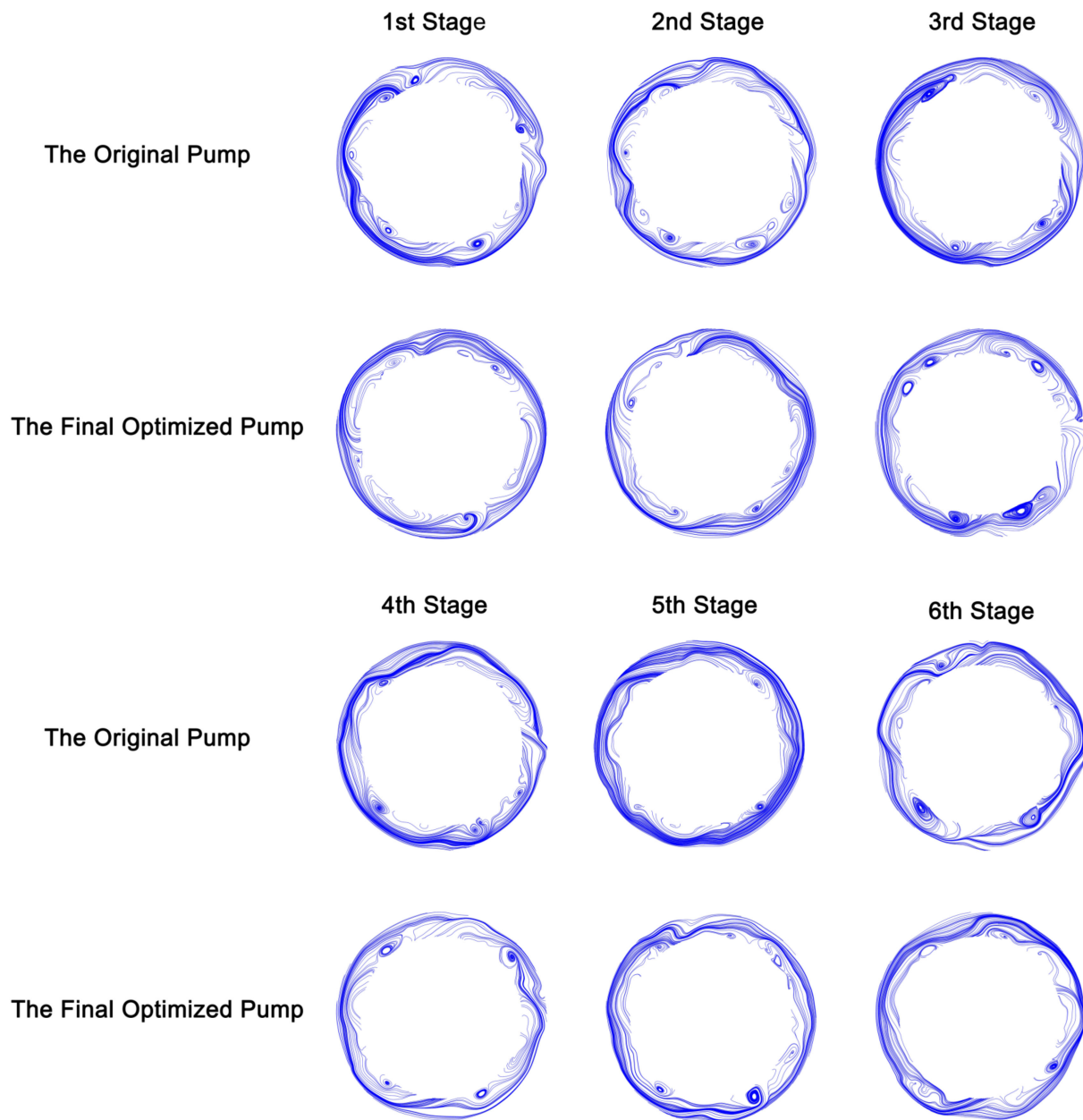
Figure 14. The streamlines on the cross-section at the transition between the impeller outlet and the diffuser inlet.

On the one hand, vortices can affect the main flow and block the flow path; on the other hand, vortices can cause significant hydraulic loss. This hydraulic loss can be measured in terms of turbulence kinetic energy loss. Figure 15 shows the turbulence kinetic energy on the cross-section at the transition between the impeller outlet and the diffuser inlet. The results show that the turbulence kinetic energy loss is significantly lower at each stage of the optimized pump.
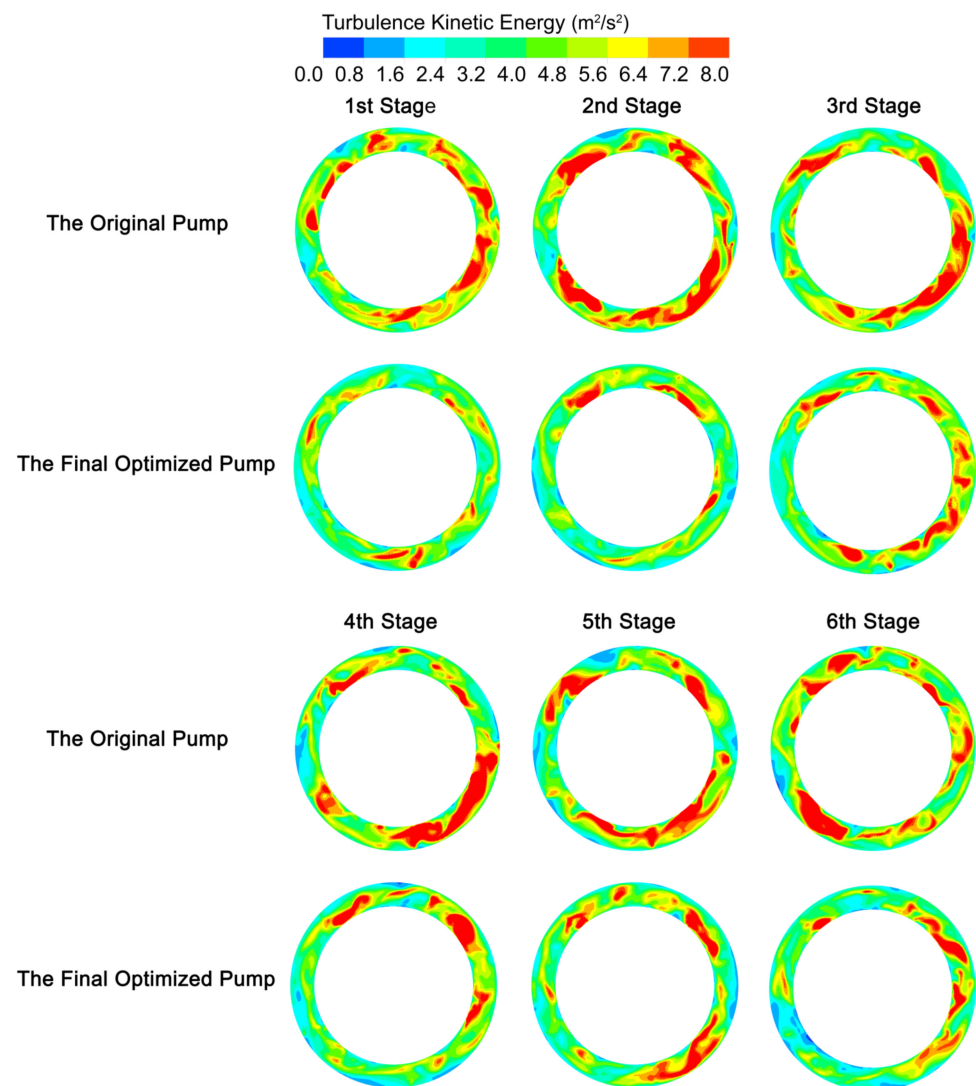
Figure 15. The turbulence kinetic energy on the cross-section at the transition between the impeller outlet and the diffuser inlet.

6.3. Comparative Analysis in Solid-Liquid Two-Phase Flow Conditions

The comparison of the hydraulic performance of the original and final optimized pump in the rated solid-liquid two-phase flow conditions (C_v = 5%,$\overline{\Phi}$= 10 mm) is shown in Table 14. Due to the increased hydraulic loss produced by the addition of solid particles, both the original pump and final optimized pump have a lower head, a greater shaft power, and a worse efficiency than under clear water conditions. However, the head of the final optimized pump still meets the design requirements, the shaft power is reduced by 113,730 W (15.64%), and the efficiency is increased by 6.00%.

Table 14. Comparison of the hydraulic performance of the original and final optimized pump in the rated solid-liquid two-phase condition.

	Head (m)	Shaft Power (W)	Efficiency (%)
The original pump	290.97	727,158	47.80
The final optimized pump	276.27	613,428	53.80

7. Conclusions

In this study, a multi-objective optimization strategy for deep-sea mining pumps based on the CFD, GABP neural network, and NSGA-III is proposed, which can significantly

enhance the hydraulic performance of deep-sea mining pumps. Summarizing all the experimental and simulated results, the following are the primary conclusions:

(1) The relative errors of the head, shaft power, and efficiency of the CFD numerical simulation under clear water conditions are within 4.87%. The relative error of the head of the CFD-DPM simulation under solid-liquid two-phase flow conditions is 3.33% at most. The numerical simulation approach is regarded as credible and can be utilized to guide the optimization of deep-sea mining pumps.

(2) The mean relative errors of the GABP neural network for the head, shaft power, and efficiency prediction were 0.31%, 0.73%, and 0.34%, respectively, which were significantly reduced compared with the BP neural network. Therefore, it is effective to enhance the prediction performance of the BP neural network by optimizing the weights and thresholds through the GA.

(3) The results of the NSGA-III multi-objective search are evenly distributed in the region of the superior overall performance of the pump. The impeller outlet width and inlet blade angle of the diffuser of the final optimized deep-sea mining pump were increased, and the average outlet diameter of the impeller and outlet blade angle of the impeller were reduced. Under rated clear water conditions, the final optimized pump has a reduction in shaft power of 100,607 W (14.65%) and an increase in efficiency of 6.04% while meeting the design requirements for the head. The flow field in the pump is significantly improved, with fewer vortices and lower turbulent kinetic energy loss. Under rated solid-liquid two-phase flow conditions, the head still meets the design requirements, the shaft power is reduced by 113,730 W (15.64%), and the efficiency is increased by 6.00%.

Author Contributions: Conceptualization, Q.H. and X.Z.; methodology, X.Z.; software, X.Z. and Q.H.; validation, Q.H., X.Z. and Z.L.; formal analysis, X.Z.; investigation, Q.H., X.Z. and Z.L.; resources, Q.H.; data curation, X.Z.; writing—original draft preparation, X.Z.; writing—review and editing, X.Z. and Q.H.; visualization, X.Z.; supervision, Q.H.; project administration, Q.H.; funding acquisition, Q.H. All authors have read and agreed to the published version of the manuscript.

Institutional Review Board Statement: Not applicable.

Informed Consent Statement: Not applicable.

Data Availability Statement: Not applicable.

Conflicts of Interest: The authors declare no conflict of interest.

Appendix A

Table A1. Design variable samples generated by the OLHS method.

D_{2m}(mm)	b_2(mm)	β_2(°)	α_3(°)
395.28	66.87	22.85	13.35
395.81	71.13	26.74	12.05
396.01	65.97	37.95	15.95
396.58	69.30	29.64	18.40
397.33	62.16	35.24	9.76
397.81	62.62	17.09	16.25

Table A1. *Cont.*

D_{2m}(mm)	b_2(mm)	β_2(°)	α_3(°)
398.42	62.43	30.74	16.69
398.89	64.12	16.19	18.22
399.12	67.58	20.68	15.64
399.73	73.97	33.36	17.36
400.25	69.07	22.94	12.72
400.63	70.06	17.79	9.60
401.36	63.16	17.99	19.82
401.86	71.00	32.80	8.66
402.23	69.80	25.90	15.28
402.56	68.50	22.20	14.51
403.08	73.02	27.46	10.16
403.86	65.69	15.74	10.84
404.44	70.63	23.34	8.44
404.62	66.71	16.74	16.47
405.36	60.47	18.34	9.31
405.53	67.45	36.71	17.88
406.29	68.42	25.12	11.23
406.95	61.49	27.74	14.28
407.28	64.76	31.18	16.01
407.75	74.12	25.72	13.65
408.05	64.46	19.45	19.23
408.69	70.39	35.57	10.36
409.08	72.95	39.92	17.56
409.84	66.12	39.40	11.11
410.05	61.79	24.82	12.82
410.85	60.89	19.62	14.18
411.31	65.09	27.92	11.80
411.63	74.37	34.77	13.53
412.12	66.29	26.27	14.94
412.70	68.76	28.89	12.47
413.15	73.72	38.36	18.89
413.53	60.15	36.08	13.85
414.41	63.80	31.70	11.58
414.72	74.74	34.32	9.07
415.36	61.22	20.98	16.86
415.75	60.73	32.95	9.86
416.11	74.93	39.08	10.55
416.76	72.07	28.47	18.05
417.24	65.28	18.82	19.42
417.80	67.80	32.32	15.16
418.35	72.49	30.21	8.20
418.83	61.66	37.32	17.04
419.05	63.70	15.08	8.85
419.53	63.43	29.23	19.16
420.22	71.72	24.41	17.73
420.74	67.09	16.28	18.75
421.03	73.45	37.80	12.28
421.52	64.67	23.98	11.63
422.22	62.94	36.66	19.71
422.74	72.00	21.40	15.42
423.36	72.72	20.26	13.11
423.56	68.10	22.08	14.77
424.17	69.61	31.43	10.75
424.83	71.42	34.05	8.26

References

1. United Nations Office of Legal Affairs; International Seabed Authority. *Marine Mineral Resources: Scientific Advances and Economic Perspectives*; United Nations: New York, NY, USA, 2004; pp. 58–62.
2. Kang, Y.J.; Liu, S.J. The Development History and Latest Progress of Deep-Sea Polymetallic Nodule Mining Technology. *Minerals* **2021**, *11*, 17. [CrossRef]
3. Deng, L.W.; Hu, Q.; Chen, J.; Kang, Y.J.; Liu, S.J. Particle Distribution and Motion in Six-Stage Centrifugal Pump by Means of Slurry Experiment and CFD-DEM Simulation. *J. Mar. Sci. Eng.* **2021**, *9*, 19. [CrossRef]
4. Hu, Q.; Chen, J.; Deng, L.W.; Kang, Y.J.; Liu, S.J. CFD-DEM Simulation of Backflow Blockage of Deep-Sea Multistage Pump. *J. Mar. Sci. Eng.* **2021**, *9*, 19. [CrossRef]
5. Kang, Y.J.; Liu, S.J.; Zou, W.S.; Zhao, H.; Hu, X.Z. Design and analysis of an innovative deep-sea lifting motor pump. *Appl. Ocean Res.* **2019**, *82*, 22–31. [CrossRef]
6. Kang, Y.; Liu, S.; Hu, X.; Dai, Y.; IEEE. Numerical and Experimental Investigation of a Multistage Electric Lifting Pump for Deep-sea Mining. In Proceedings of the 3rd International Conference on Smart City and Systems Engineering (ICSCSE), Xiamen, China, 28–30 December 2018; pp. 457–462.
7. Oh, H.W.; Chung, M.K. Optimum values of design variables versus specific speed for centrifugal pumps. *Proc. Inst. Mech. Eng. Part A-J. Power Energy* **1999**, *213*, 219–226. [CrossRef]
8. Oh, H.W.; Kim, K.Y. Conceptual design optimization of mixed-flow pump impellers using mean streamline analysis. *Proc. Inst. Mech. Eng. Part A-J. Power Energy* **2001**, *215*, 133–138. [CrossRef]
9. Yang, J.H.; Bian, Z.; Zhong, C.L.; Li, J.C. Method for Selecting Centrifugal Pump Impeller Outlet Angle Based on Calculation of Centrifugal Pump Impeller's Hydraulic Loss. *J. Xi Hua Univ.* **2016**, *35*, 89.
10. Pei, J.; Yin, T.Y.; Yuan, S.Q.; Wang, W.J.; Wang, J.B. Cavitation optimization for a centrifugal pump impeller by using orthogonal design of experiment. *Chin. J. Mech. Eng.* **2017**, *30*, 103–109. [CrossRef]
11. Ayremlouzadeh, H.; Jafarmadar, S.; Niaki, S.R.A. Investigation on the Effect of Impeller Design Parameters on Performance of a Low Specific Speed Centrifugal Pump Using Taguchi Optimization Method. *Int. J. Fluid Power* **2022**, *23*, 161–182. [CrossRef]
12. Heo, M.W.; Kim, K.Y.; Kim, J.H.; Choi, Y.S. High-efficiency design of a mixed-flow pump using a surrogate model. *J. Mech. Sci. Technol.* **2016**, *30*, 541–547. [CrossRef]
13. Hong, S.; Hu, X. Optimization of impeller of deep-sea mining pump for erosive wear reduction based on response surface methodology. *Mar. Georesources Geotechnol.* **2022**, 1–17. [CrossRef]
14. Coello, C.A.C. Evolutionary multi-objective optimization: Some current research trends and topics that remain to be explored. *Front. Comput. Sci. China* **2009**, *3*, 18–30. [CrossRef]
15. Marler, R.T.; Arora, J.S. Survey of multi-objective optimization methods for engineering. *Struct. Multidiscip. Optim.* **2004**, *26*, 369–395. [CrossRef]
16. von Lucken, C.; Baran, B.; Brizuela, C. A survey on multi-objective evolutionary algorithms for many-objective problems. *Comput. Optim. Appl.* **2014**, *58*, 707–756. [CrossRef]
17. Nourbakhsh, A.; Safikhani, H.; Derakhshan, S. The comparison of multi-objective particle swarm optimization and NSGA II algorithm: Applications in centrifugal pumps. *Eng. Optim.* **2011**, *43*, 1095–1113. [CrossRef]
18. Gan, X.; Pei, J.; Wang, W.; Yuan, S.; Lin, B. Application of a modified MOPSO algorithm and multi-layer artificial neural network in centrifugal pump optimization. *Eng. Optim.* **2022**, 1–19. [CrossRef]
19. Gan, X.; Wang, W.; Pei, J.; Yuan, S.; Tang, Y.; Osman, M.K. Direct Shape Optimization and Parametric Analysis of a Vertical Inline Pump via Multi-Objective Particle Swarm Optimization. *Energies* **2020**, *13*, 425. [CrossRef]
20. Zhang, J.Y.; Zhu, H.W.; Yang, C.; Li, Y.; Wei, H.A. Multi-objective shape optimization of helico-axial multiphase pump impeller based on NSGA-II and ANN. *Energy Convers. Manag.* **2011**, *52*, 538–546. [CrossRef]
21. Shojaeefard, M.H.; Hosseini, S.E.; Zare, J. CFD simulation and Pareto-based multi-objective shape optimization of the centrifugal pump inducer applying GMDH neural network, modified NSGA-II, and TOPSIS. *Struct. Multidiscip. Optim.* **2019**, *60*, 1509–1525. [CrossRef]
22. Xu, K.; Wang, G.; Zhang, L.Y.; Wang, L.Q.; Yun, F.H.; Sun, W.H.; Wang, X.Y.; Chen, X. Multi-Objective Optimization of Jet Pump Based on RBF Neural Network Model. *J. Mar. Sci. Eng.* **2021**, *9*, 18. [CrossRef]
23. Gandhi, B.K.; Singh, S.N.; Seshadri, V. Effect of Speed on the Performance Characteristics of a Centrifugal Slurry Pump. *J. Hydraul. Eng.* **2002**, *128*, 225–233. [CrossRef]
24. Celik, I.B.; Ghia, U.; Roache, P.J.; Freitas, C.J. Procedure for estimation and reporting of uncertainty due to discretization in CFD applications. *J. Fluids Eng. -Trans. Asme* **2008**, *130*, 078001. [CrossRef]
25. Feng, J.; Luo, X.; Guo, P.; Wu, G. Influence of tip clearance on pressure fluctuations in an axial flow pump. *J. Mech. Sci. Technol.* **2016**, *30*, 1603–1610. [CrossRef]
26. Zhang, N.; Yang, M.; Gao, B.; Li, Z.; Ni, D. Investigation of Rotor-Stator Interaction and Flow Unsteadiness in a Low Specific Speed Centrifugal Pump. *Stroj. Vestn. -J. Mech. Eng.* **2016**, *62*, 22–31. [CrossRef]
27. Shields, M.D.; Zhang, J. The generalization of Latin hypercube sampling. *Reliab. Eng. Syst. Saf.* **2016**, *148*, 96–108. [CrossRef]
28. Basheer, I.A.; Hajmeer, M. Artificial neural networks: Fundamentals, computing, design, and application. *J. Microbiol. Methods* **2000**, *43*, 3–31. [CrossRef]

29. Deb, K. Multi-objective Genetic Algorithms: Problem Difficulties and Construction of Test Problems. *Evol. Comput.* **1999**, *7*, 205–230. [CrossRef]

30. Deb, K. An efficient constraint handling method for genetic algorithms. *Comput. Methods Appl. Mech. Eng.* **2000**, *186*, 311–338. [CrossRef]

31. Deb, K.; Pratap, A.; Agarwal, S.; Meyarivan, T. A fast and elitist multiobjective genetic algorithm: NSGA-II. *IEEE Trans. Evol. Comput.* **2002**, *6*, 182–197. [CrossRef]

32. Deb, K.; Jain, H. An Evolutionary Many-Objective Optimization Algorithm Using Reference-Point-Based Nondominated Sorting Approach, Part I: Solving Problems With Box Constraints. *IEEE Trans. Evol. Comput.* **2014**, *18*, 577–601. [CrossRef]

33. Jain, H.; Deb, K. An Evolutionary Many-Objective Optimization Algorithm Using Reference-Point Based Nondominated Sorting Approach, Part II: Handling Constraints and Extending to an Adaptive Approach. *IEEE Trans. Evol. Comput.* **2014**, *18*, 602–622. [CrossRef]